Journal of *Marine Science and Engineering*

MDPI

Article

Modelling Coastal Flooding Induced by Wave Overtopping Using SCHISM Coupled with EurOtop

Hyeok Jin, JongJib Park *, SuYoung Jeong and HeungBae Choi

Department of Forecast, Geosystem Research Inc., 172 LS-ro, Gunpo 15807, Republic of Korea; hyeokjin@geosr.com (H.J.); syjeong@geosr.com (S.J.); hbchoi@geosr.com (H.C.)
* Correspondence: jjpark@geosr.com; Tel.: +82-31-5180-5863

Abstract

Coastal cities protected by artificial structures are vulnerable to wave overtopping during typhoons, where flooding can occur even when the still water level stays below the structure crest. This study develops EurOtop-based wave overtopping modules within the cross-scale SCHISM-WWM modelling framework and applies the coupled model to Marine City, Busan, South Korea. At each time step, the module extracts the local water level and wave conditions at a coastal-structure pair-node, computes the overtopping or overflow discharge from the EurOtop formulae while accounting for wave direction, roughness reduction, and crest-width transfer losses, and injects it as a landward source term for inland flood propagation. The framework is evaluated against two typhoon events. For Typhoon Hinnamnor in 2022, comparison with the CCTV-based overtopping record reproduces the timing and intensity of overtopping. For Typhoon Chaba in 2016, validation against field-surveyed inundation marks shows that the modelled maximum inundation depth matches the observed spatial pattern and the survey-point observations to within a mean absolute difference of about 12 cm. These results demonstrate the framework's applicability to overtopping-induced compound flooding in urbanised coastal cities and, since it is fully coupled within the SCHISM-WWM codebase, its capacity to incorporate further drivers such as pluvial and fluvial flooding.

Keywords: wave overtopping; coastal flooding; compound flooding; inundation; coupled model; SCHISM; WWM; EurOtop

1. Introduction

Coastal flooding during extreme typhoons has become an increasing concern in densely urbanised coastal regions, where natural shorelines have often been replaced by seawalls, dikes, breakwaters, and other artificial coastal defenses. Although these structures are designed to protect inland areas from direct wave attack and storm surge, wave overtopping can still induce severe flooding even when the still water level remains below the crest elevation [1,2]. Unlike overflow, which is mainly governed by the exceedance of water level over the crest, wave overtopping is strongly controlled by the combined effects of wave height, wave period, wave direction, freeboard, and the geometric characteristics of coastal structures. Therefore, accurate simulation of overtopping-induced coastal flooding requires a modelling approach that can represent not only local wave and storm-surge conditions but also local structure-dependent overtopping processes and the subsequent propagation of overtopped water into inland areas.

Check for updates

Academic Editor: Isavela N. Monioudi

Received: 26 June 2026
Revised: 16 July 2026
Accepted: 22 July 2026
Published: 24 July 2026

Copyright: © 2026 by the authors. Licensee MDPI, Basel, Switzerland. This article is an open access article distributed under the terms and conditions of the Creative Commons Attribution (CC BY) license.

In principle, wave overtopping can be most explicitly simulated using phase-resolving or computational fluid dynamics (CFD) models, which resolve wave–structure interaction, run-up, impact, turbulence, and overtopping jets [3]. A recent comparison with physical model measurements showed that both CFD and non-hydrostatic modelling approaches satisfactorily reproduced the physics of spectral evolution and wave overtopping, although some quantitative underprediction remained in the non-hydrostatic results [4]. However, their use is often impractical for applications that require rapid results, such as coastal flood forecasting, or for applications that require repeated simulations, such as climate change impact assessments and hypothetical typhoon scenario experiments. This limitation arises from their high computational cost and restricted domain size. Because such models generally cannot cover the full offshore-to-inland flood domain, regional hydrodynamic and wave models must often be run separately to provide boundary conditions for local overtopping simulations [5], introducing additional computational burden and boundary-transfer uncertainty [6]. Meanwhile, hybrid deep-learning surrogate models can substantially reduce the computational cost of flood prediction after training. For example, a recent CNN–LSTM surrogate model reduced the computational time for each flood event from 4–6 h with a physics-based hydrodynamic model to approximately 3.2 min while reproducing the spatial extent and temporal evolution of urban flooding [7]. However, the reliability and transferability of AI- and machine-learning-based flood models remain dependent on the coverage and quality of the available data, and their predictions for locations or conditions outside the training domain remain uncertain [8]. Therefore, empirical wave overtopping formulae have been coupled with hydrodynamic–wave models as a practical alternative for estimating overtopping discharge and simulating overtopping-driven coastal flooding at regional to urban scales.

Several studies [1,2,9–12] have attempted to incorporate empirical wave overtopping formulations into coastal inundation models. SuWAT-SWAN-IFORM [1,9] is a representative structured-grid-based system that combines hydrodynamic, wave, and overtopping models for overtopping-induced coastal flooding. A key feature of this approach is that overtopping discharge is not necessarily estimated from wave conditions immediately at the structure toe, where wave transformation after breaking may be uncertain in phase-averaged wave models such as SWAN. Instead, wave conditions at more stable offshore or breaking-depth locations are used to estimate overtopping discharge. This approach is useful for reducing uncertainty associated with near-structure wave inputs. However, because the system is based on nested structured grids, model errors may propagate through sequential boundary forcing from outer to inner domains. In addition, structured grids are less flexible in smoothly representing complex coastal geometries, such as irregular shorelines, harbor basins, narrow channels, and nonuniform coastal defenses.

TELEMAC/TOMAWAC-EurOtop [10,11] has also been applied to overtopping-induced coastal flood modelling by introducing EurOtop-based discharge into a two-dimensional hydrodynamic model. Unlike structured-grid systems, TELEMAC/TOMAWAC employs an unstructured-grid framework, which provides greater flexibility for representing irregular shorelines. However, in this framework, overtopping discharge is imposed at single injection nodes assigned to coastal structure sections with similar geometric characteristics. Consequently, the number and spatial arrangement of these injection nodes can become sensitive factors influencing the distribution of overtopping inflow, inland flow pathways, local flood depths, and overall inundation extent.

ADCIRC/UnSWAN-EurOtop [2,12] has been applied to unstructured-grid overtopping-driven coastal flood modelling by estimating overtopping discharge along coastal-structure pair-lines and transferring it into the inundation domain. This approach provides a more flexible representation of structure-aligned overtopping inflow than single-node source

methods. However, previous applications employed two-dimensional, depth-averaged barotropic storm surge–wave–inundation frameworks. Such configurations are well suited for simulating surge, wave overtopping, and inundation during the main storm period but do not represent three-dimensional baroclinic and large-scale ocean-adjustment processes that can influence post-storm water-level recovery and flood persistence. For instance, baroclinic effects can influence water-level adjustment following the main storm-surge peak and subsequent compound-flooding events [13], and post-storm oceanic adjustment can maintain elevated coastal water levels and thereby contribute to delayed inundation [14]. Extending overtopping-driven flood modelling toward cross-scale compound flooding therefore requires a framework that can connect offshore, nearshore, estuarine, riverine, and inland domains while allowing future extension to three-dimensional baroclinic simulations.

To address these requirements, this study adopts the SCHISM-WWM framework [15,16] for overtopping-driven coastal flood modelling. SCHISM is an unstructured-grid, cross-scale hydrodynamic model that can connect offshore, nearshore, estuarine, riverine, and inland flood domains within a single computational mesh. In addition, SCHISM can flexibly support two-dimensional barotropic and three-dimensional baroclinic configurations, either as standalone setups or as mixed configurations within a single unstructured grid, depending on the dominant physical processes and modelling objectives. This flexibility provides a pathway for future compound flooding studies that consider post-storm water-level adjustment and flood persistence. Coupled with WWM, the framework can dynamically provide the water levels, significant wave heights, wave periods, and wave directions required for overtopping estimation.

Building on this coupled framework, a EurOtop-based module was incorporated to compute overtopping and overflow discharges at individual coastal-structure pair-nodes. At each model time step, the module uses local wave conditions and water levels together with structure-specific information, thereby accounting for spatial variations in both hydrodynamic forcing and structural characteristics along the coastal structure. Structure-type-dependent EurOtop formulae are implemented to represent both sloping and vertical coastal defenses, and the computed discharge is transferred into the inland flood domain as a source term for subsequent inland flood propagation. Through this approach, the model aims to represent the spatial variability of overtopping inflow along complex coastal structures and its contribution to inland flooding. The model is applied to Marine City, Busan, South Korea, and evaluated using two historical typhoon events, Typhoon Chaba (2016) and Typhoon Hinnamnor (2022). The objective of this study is to develop and validate a EurOtop-based overtopping module within SCHISM-WWM by reconstructing historical typhoon-induced overtopping and coastal flooding events. The validated framework is intended to provide a basis for future scenario-based coastal flood-risk analyses and potential extension to operational forecasting.

2. Model Development

2.1. Coupling Framework

In the coupled SCHISM-WWM system, SCHISM [15] is a three-dimensional, unstructured-grid hydrodynamic model and WWM [16] is a spectral wave model run on the same grid, while the overtopping module is responsible for estimating the discharge at the structure front. After initialisation, SCHISM is forced by surface wind and sea-level pressure fields obtained from an external atmospheric analysis dataset and interpolated in space and time onto the model grid. From these fields, the model computes the surface wind stress and the atmospheric pressure-gradient forcing. The same wind field forces WWM, which computes the wave field from the wave action spectrum equations, Equations (1) and (2).

In these equations, N denotes the wave action density, which is defined as a function of time t, the spatial coordinate X, the relative frequency σ, and the wave direction θ. The wave action density is obtained by dividing the wave energy density E by the relative frequency σ, and S_{tot} represents the source/sink term that accounts for the effects of wind input, wave breaking, and bottom friction. Calculated wave information (wave height, period, and direction) is then used by the overtopping module to compute the overtopping discharge. On the landward side, the three-dimensional continuity equation, Equation (3), updates the water level. Here, $\vec{u}$ denotes the velocity vector in the horizontal direction, while w is the velocity component in the vertical direction, and $S(x,y,t)$ is the source term, which corresponds to the overtopping inflow per unit surface area. This equation updates the water level by taking the calculated overtopping as a source term, after which the momentum equation and the wetting-and-drying algorithm compute the velocity field and the new water levels in the previously dry domain. These sequences, shown in Figure 1, are repeated at every computational step.

$$\frac{\partial}{\partial t}N + \nabla(XN) + \frac{\partial}{\partial \sigma}(\theta N) + \frac{\partial}{\partial \theta}(\sigma N) = S_{tot} \quad (1)$$

$$N(t, X, \sigma, \theta) = \frac{E(t, X, \sigma, \theta)}{\sigma} \quad (2)$$

$$\nabla \cdot \vec{u} + \frac{\partial w}{\partial z} = S(x, y, t) \quad (3)$$

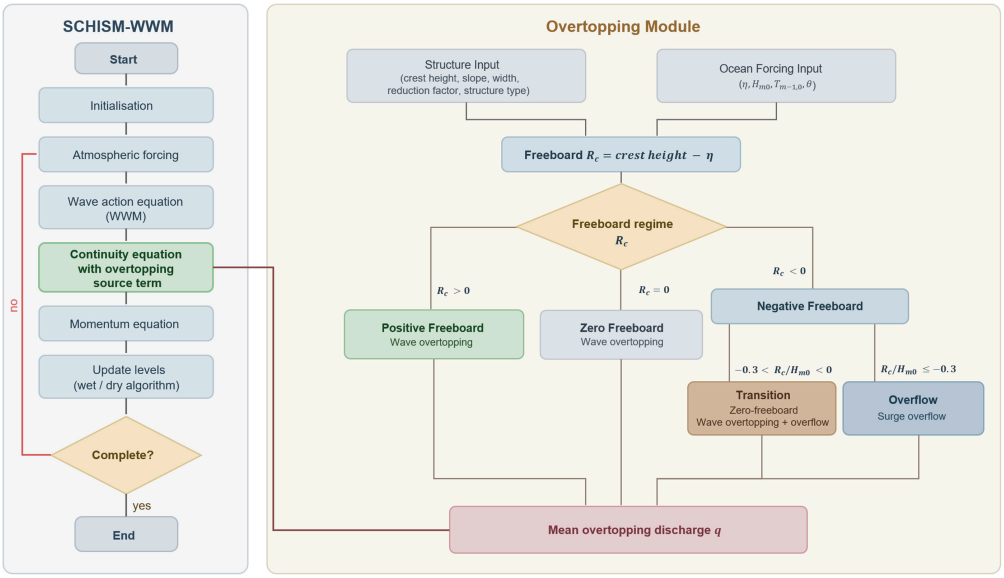


Figure 1. Schematic flow of the wave-overtopping module integrated into the SCHISM-WWM coupling loop.

Figure 2 conceptually illustrates, from the perspective of the grid system, the overall process by which the overtopping discharge is applied as a source term within the SCHISM grid and delivered to the inundation domain. Each sea-side node defined along the coastal structure is indexed as $j = 1, \ldots, n$ and paired with the corresponding inland node j'. At each overtopping update, the water level, wave height, wave period, and wave direction at sea-side node j are obtained from SCHISM–WWM. These local conditions are used to compute the mean overtopping discharge per unit crest width (q_j). Consequently, q_j is calculated separately for each pair and varies along the structure according to the local hydrodynamic and wave conditions. The representative spacing $dist_j$ associated with pair j is reconstructed from the surrounding mesh-side lengths along the sea and inland sides of

the structure. If side lengths are available on both sides, $dist_j$ is taken as their arithmetic mean. Since q_j is expressed per unit crest width, the volumetric rate associated with pair j is $q_j dist_j$. The total overtopping discharge (q_{total}) across the structure is calculated as $q_{total} = \sum_{j=1}^{n} q_j dist_j$. Consequently, the total discharge delivered to the inundation domain remains independent of the grid resolution along the structure. A finer node spacing distributes the same total flow across a larger number of nodes, whereas a coarser spacing allocates a proportionally greater flow to each node. In either case, the integrated overtopping volume is conserved. During each water-level time step (Δt), the volumetric rate $q_j dist_j$ is distributed equally between the two end nodes of each mesh side, yielding right-hand-side contributions to the continuity equation (Equation (3)) of $-\Delta t\left(q_j dist_j\right)/2$ at the sea-side nodes and $+\Delta t\left(q_j dist_j\right)/2$ at the paired inland nodes. The factor $1/2$ accounts for the equal distribution from a mesh side to its two end nodes, whereas the opposite signs ensure that the overtopping volume removed from the sea side is added to the inland side, thereby conserving the total water volume.

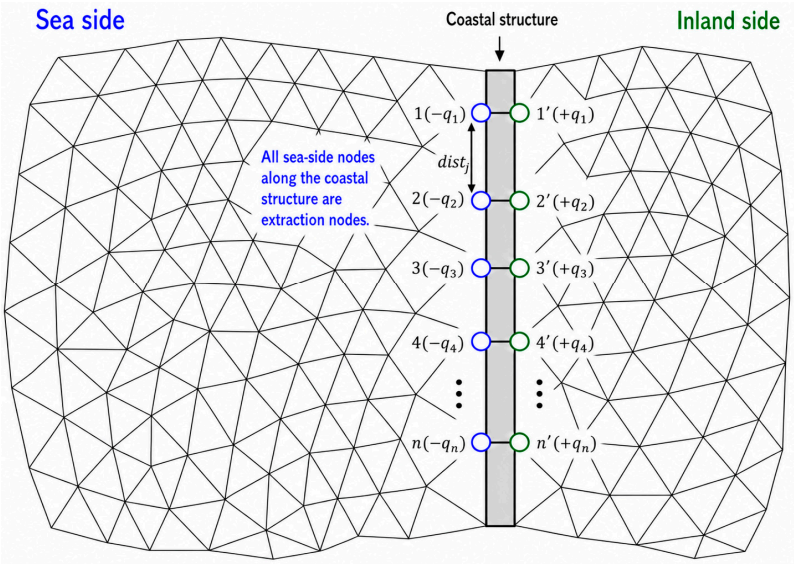


Figure 2. Pair-node representation of a coastal structure on the unstructured grid.

2.2. Overtopping Module

2.2.1. EurOtop (2018) [17]

EurOtop (2018) is an empirically based manual for estimating mean wave overtopping discharge (q) at coastal defenses, generalised from a database of more than 13,000 physical model tests. The mean discharge depends jointly on the incident wave conditions and the geometric and surface characteristics of the structure, which are incorporated as empirical coefficients and key structural parameters in the overtopping formulae. The EurOtop formulae calculate the mean overtopping discharge per unit crest width averaged over a sequence of waves, rather than the instantaneous discharge associated with an individual overtopping event.

EurOtop is not a single equation but encompasses various equations from which the appropriate formula is selected according to the forcing conditions and the structure type. The present module classifies structures as sloping or vertical and distinguishes wave conditions by breaking or non-breaking behaviour, impulsive or non-impulsive loading, and positive or negative freeboard. The structure type, slope, crest level, width, orientation, and roughness class are defined in the input file, and each pair-node references the attributes. As illustrated by the freeboard regimes in Figure 1, the mean overtopping discharge is evaluated by one of three representative relations according to the relative freeboard

R_c/H_{m0}: wave overtopping for a positive freeboard, a transition phase combining wave overtopping and overflow, and surge overflow given by Equations (4)–(6), respectively.

$$q/\sqrt{gH_{m0}{}^3} = a\exp[-(b\cdot R_c/H_{m0})^c],\ R_c > 0 \quad (4)$$

$$q = a\sqrt{gH_{m0}{}^3} + 0.54\sqrt{g|R_c|^3}, -0.3 < R_c/H_{m0} \leq 0 \quad (5)$$

$$q = 0.54\sqrt{g|R_c|^3},\ R_c/H_{m0} \leq -0.3 \quad (6)$$

In Equations (4)–(6), H_{m0} is the spectral significant wave height, R_c the freeboard, g the gravitational acceleration, and a, b, and c are empirical coefficients that depend on the structure type and the breaking and wave obliquity conditions. For a positive freeboard ($R_c > 0$), the discharge is governed by wave overtopping (Equation (4)) and decreases exponentially as the crest rises above the still water level. In the transition phase ($-0.3 < R_c/H_{m0} \leq 0$), where the crest is slightly submerged, both wave overtopping and steady overflow contribute simultaneously. Several approaches have been proposed for this combined regime [1,17,18], and the present module adopts the method of the EurOtop manual [17], in which the combined discharge (Equation (5)) is obtained by superposing the zero-freeboard wave-overtopping component, given by Equation (4) evaluated at $R_c = 0$, and the surge-overflow component of Equation (6). For a more negative freeboard ($R_c/H_{m0} \leq -0.3$), the crest is sufficiently submerged that wave-driven overtopping becomes negligible and the discharge is dominated by weir-type surge overflow (Equation (6)), evaluated from the submergence depth $|R_c|$.

2.2.2. Wave Direction Effect

Wave overtopping is affected by the direction from which waves approach a coastal structure. The discharge is largest when waves are incident normal to the structure and decreases as the obliquity of incidence increases, so that neglecting the wave-direction effect can lead to a substantial overestimation of overtopping for obliquely incident waves. This directional attenuation is governed by the difference between the orientation of the structure and the angle of wave incidence. Because the wave direction can vary rapidly under extreme conditions such as typhoons, it is important to reflect it in real time during the dynamic computation. Jo et al. [9] performed numerical experiments at Kansai International Airport, Japan, accounting for the effect of wave direction, and quantitatively demonstrated that the wave direction substantially affects the magnitude of the overtopping discharge.

To reflect the wave direction effect within the model, the present module computes the wave incident angle at every computational step by comparing the wave direction calculated by WWM at each extraction node with the structure orientation derived from the geometry of the corresponding pair-node. The structure orientation is defined from the line connecting the seaward and landward nodes of each pair. The relative angle β is then obtained at each extraction node as the difference between the WWM wave direction and this structure orientation (Figure 3), and the influence factor for the wave direction γ_β corresponding to β is applied to the computed discharge. Equation (7) is applied for smooth, impermeable structures, including vertical walls. For permeable rubble mound slopes, Equation (8) is applied, for which the effect of wave direction is stronger and γ_β decreases more steeply with β. The overtopping module selects the appropriate relation according to the structure type assigned to each pair-node. Because β is evaluated independently for each pair-node at every time step, the along-shore variation of structure orientation and the temporal evolution of the incident wave direction are both resolved,

allowing the spatial distribution of overtopping along a coastline of varying orientation to be represented consistently.

$$\gamma_\beta = 1 - 0.0033|\beta| \text{ for } 0^\circ \leq |\beta| \leq 80^\circ,\ \gamma_\beta = 0.736 \text{ for } \left|\beta\right| > 80^\circ \quad (7)$$

$$\gamma_\beta = 1 - 0.0063\left|\beta\right| \text{ for } 0^\circ \leq \left|\beta\right| \leq 80^\circ,\ \gamma_\beta = 0.496 \text{ for } \left|\beta\right| > 80^\circ \quad (8)$$

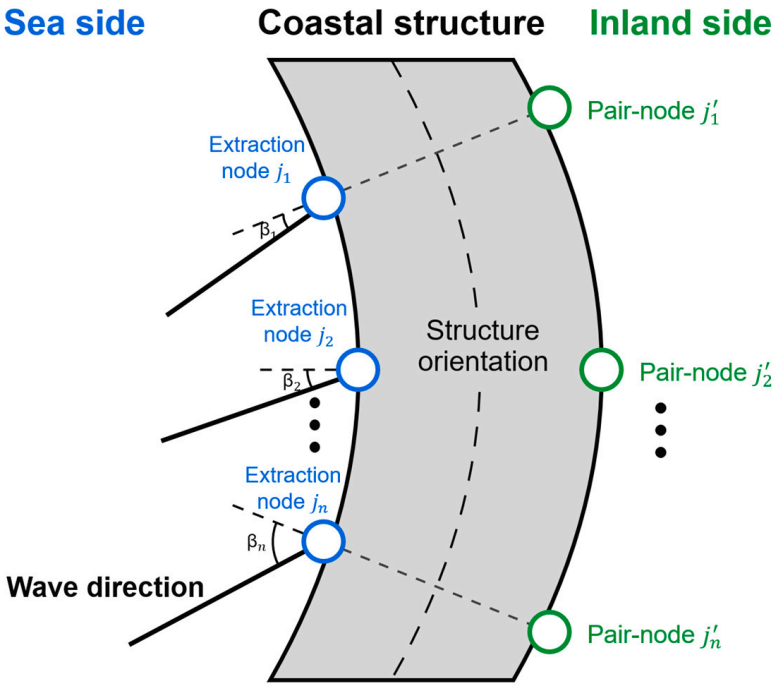


Figure 3. Definition of the relative angle β between the incident wave direction and the structure orientation at each pair-node.

2.2.3. Roughness and Reduction Factor

For rubble mound structures, the rough, permeable armour layer dissipates wave energy and reduces overtopping over the crest. EurOtop accounts for this through the roughness reduction factor (γ_f) to lower the predicted overtopping discharge. The reduction, however, is influenced by the wave period, or equivalently the wave steepness, since longer-period, lower-steepness waves run up farther and overtop more readily, thereby weakening the effective roughness reduction [19]. EurOtop (2018) considers this influence only in part, allowing the factor to vary with the wave period, but restricting this variation to cases where the breaker parameter ($\xi_{m-1,0} = \tan\alpha / \sqrt{s_{m-1,0}}$) exceeds 5, so that for most sea states, the constant tabulated value is effectively applied [17]. Consequently, as the wave period increases, retaining this fixed tabulated value tends to underestimate the resulting overtopping. Eldrup et al. [20] showed, on the basis of new and existing flume data, that the wave steepness influences the roughness factor across the full range of conditions rather than only above the threshold, and that the front-slope angle should be accounted for explicitly. To account for this, the roughness factor is adjusted as a function of the wave steepness and front-slope angle following Eldrup et al. [20], as given by Equation (9):

$$\gamma_{fs} = \min\left(\gamma_f + 0.05 s_{m-1,0}^{-0.5} - 0.07 \min(\cot\alpha, 3) - 0.09, 1\right) \quad (9)$$

where γ_f is the nominal armour roughness factor from EurOtop, the front-slope steepness (cot α), and the wave steepness at the toe of the structure ($s_{m-1,0} = 2\pi H_{m0} / g T_{m-1,0}^2$). The formulation retains the EurOtop armour values as a baseline while allowing the factor to

vary with the local sea state, and is bounded above by the smooth-slope limit ($\gamma_{fs} = 1$). In the coupled model, H_{m0} and $T_{m-1,0}$ are obtained from the WWM model, so that γ_{fs} is updated dynamically at each coupling step rather than held fixed. This adjusted roughness factor is applied only under non-breaking-wave conditions, the regime for which the guidance of Eldrup et al. [20] was derived. For breaking waves, the nominal roughness factor γ_f tabulated in EurOtop is used directly. No fixed threshold is used to distinguish between breaking and non-breaking wave conditions at the extraction node. Instead, the EurOtop breaking-wave and non-breaking upper-limit relations are evaluated at each pair-node and coupling step using the local wave and structural conditions, and the regime yielding the lower overtopping discharge is selected. Therefore, the applicable regime may change over time as the local wave conditions evolve.

2.3. Crest Width Treatment for Overtopping Discharge

2.3.1. Flat Crest Structures

For flat, impermeable, or road-like crests, the overtopping flow runs along the crest and is driven by the hydraulic gradient between the seaward and landward sides. The overtopping discharge (q) estimated from EurOtop is interpreted as the potential overtopping generated at the structure front, whereas the flow actually injected at the receiving node is reduced by the attenuation that occurs as the water travels across the crest. To obtain this adjusted discharge, the hydraulic-gradient-based transfer algorithm of Lee and Suh (2016) [2] is applied. Assuming the overtopping flow to be initially uniform, the water depth along the crest is computed by stepping the energy (head-loss) equation, Equation (10), from the seaward (upstream) end to the landward (downstream) end of the structure, where y is the water depth, q the discharge per unit width, A the cross-sectional area, α the energy coefficient, z the bed elevation, g the gravitational acceleration, Δx the crest width, and S_f the friction slope. The friction slope is evaluated from Manning's relation, $S_f = V^2 n^2 / R^{4/3}$, with V flow velocity, n the roughness coefficient, and R the hydraulic radius.

$$y_1 + \alpha q^2/(2gA_1^2) + z_1 = y_2 + \alpha q^2/\left(2gA_2^2\right) + \frac{1}{2}(S_{f1} + S_{f2})\Delta x + z_2 \quad (10)$$

$$y = \left(q/\sqrt{2g}\right)^{2/3},\ V = \sqrt{2gy},\ q = AV \quad (11)$$

Subscripts 1 and 2 denote the seaward and landward crest sections, respectively. The depth–velocity relations used in the stepping are given by Equation (11). As summarised in Figure 4, the depth is computed segment by segment from the seaward to the landward end of the crest (outer loop); within each segment, starting from an assumed downstream depth, Equation (10) is solved iteratively with the Newton–Raphson method (inner loop) until the difference between the computed and assumed depths converges below a tolerance of 0.001 m, following the concept of the standard step method. The converged downstream depth then yields the adjusted overtopping discharge q' delivered to the landward node. Just as the discharge is attenuated by the roughness reduction factor (γ_{fs}) within the overtopping formulae, the adjusted discharge q' is applied at each pair-node as both the seaward sink and the landward source, thereby conserving mass by removing q' from the seaward and adding the same amount to the corresponding landward node. A wider crest lengthens the flow path and accumulates more friction and head loss, producing a larger reduction in discharge, whereas for a very narrow crest the transfer distance is short and the hydraulic-gradient correction has only a limited effect. This crest-transfer correction is applied only for a positive freeboard ($R_c > 0$). For zero or negative freeboard ($R_c \leq 0$), the flow over the crest is a continuous overflow rather than a thin overtopping layer, so

the EurOtop overflow discharge is delivered directly to the landward node without the hydraulic gradient correction.

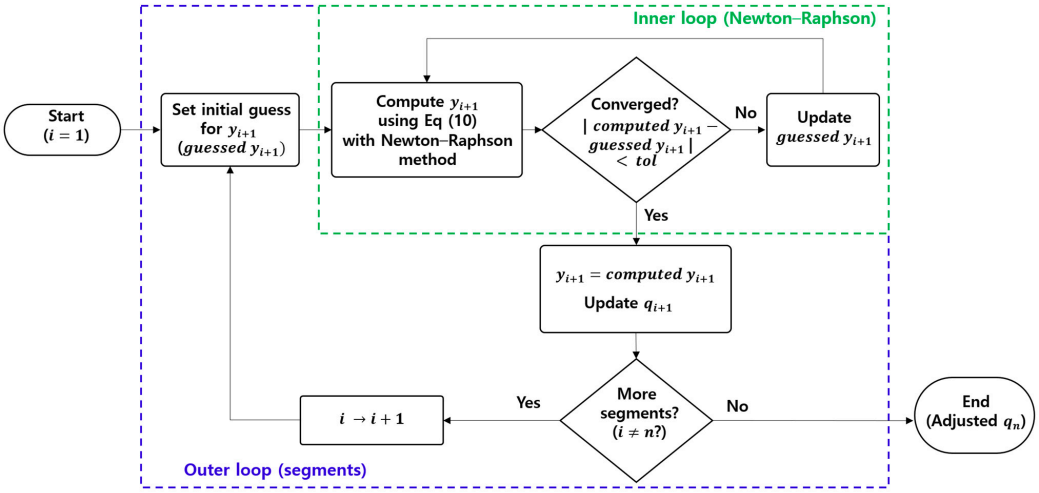


Figure 4. Flowchart of the hydraulic gradient algorithm for flat crest structures.

2.3.2. Rubble Mound Structures

A wider structure crest dissipates more of the overtopping flow before it reaches the rear shoulder and thus reduces the overtopping discharge. In EurOtop, this effect is described by the reduction factor of Besley (1999) [21], applied as a direct multiplier (C_r) on the calculated discharge (q), as given in Equation (12):

$$C_r = \min\left(3.06\exp(-1.5\frac{G_c}{H_{m0}}), 1\right) \quad (12)$$

where G_c is the crest width. Although this expression reproduces the data well within its calibration range, applying it as a constant multiplier on the calculated overtopping rate is not physically consistent at low freeboards: it implies that a wider crest still reduces overtopping even when the crest level coincides with the still water level ($R_c = 0$), whereas in that case, the influence of the crest width should be negligible.

To remove this inconsistency, the crest width effect is instead introduced as an influence factor γ_{cw} acting on the relative freeboard, following Eldrup et al. [20], so that the overtopping curves correctly converge as the relative freeboard approaches zero with the crest-width factor (Equation (13)).

$$\gamma_{cw} = \min\left(1.1\exp(-0.18\frac{G_c}{H_{m0}}), 1\right) \quad (13)$$

This formulation makes the influence of the crest width depend on the freeboard rather than scaling the discharge directly, and it is bounded above by $\gamma_{cw} = 1$ for narrow crests. Although Equation (13) was strictly validated under non-breaking-wave conditions, for relative crest widths in the range ($0 \leq G_c/H_{m0} \leq 5.18$), the crest width still attenuates the overtopping flow under breaking waves. This is consistent with the original crest width factor (C_r) of Besley (1999) [21], which is applied as a reduction on the overtopping discharge computed under either breaking or non-breaking conditions, reducing it in proportion to the crest width. The adjusted crest width factor (γ_{cw}) is therefore applied across both regimes so that the geometric influence of the crest width is consistently accounted for.

3. Study Area and Typhoon Events

3.1. Study Area: Marine City, Busan, South Korea

Marine City, located in Haeundae-gu, Busan, South Korea, is a reclaimed multi-use coastal district bordered by Suyeong Bay to the south and Haeundae Beach to the north. Situated in the vicinity of several prominent coastal landmarks, the district is densely built up with high-rise residential and commercial buildings, which renders it highly exposed to typhoon- and storm-induced coastal hazards. The sea area fronting Marine City is an open coast with water depths exceeding approximately 10 m, so that high waves combined with storm surge can readily generate wave overtopping at the coastal defenses. The district has repeatedly suffered overtopping-induced damage to its waterfront roads and structures during past typhoons, including Typhoons Maemi (2003), Bolaven (2012), Sanba (2012), and Maysak (2020) (Figure 5).

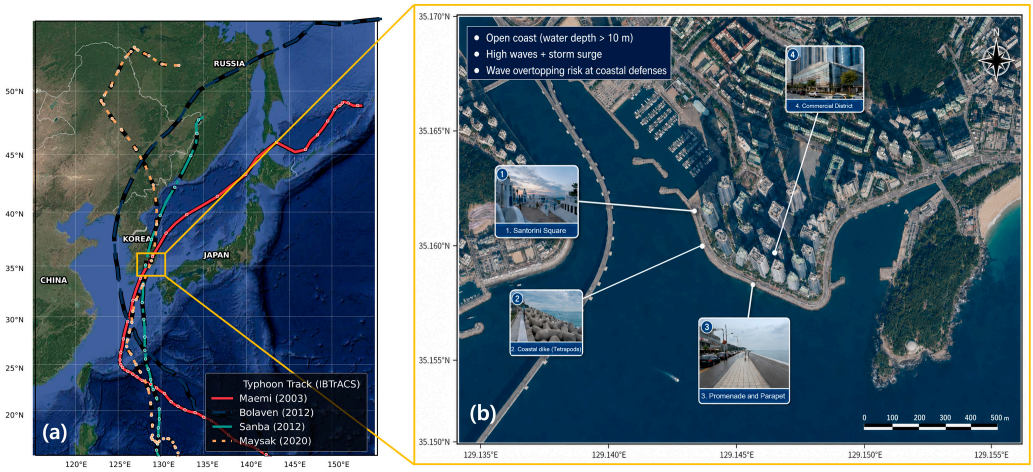


Figure 5. (**a**) Typhoon tracks causing wave overtopping in the study area (Maemi (2003), Bolaven (2012), Sanba (2012), and Maysak (2020)); (**b**) Study area and coastal infrastructure of Marine City, Busan, South Korea.

The coastal dike fronting Marine City is a sloping structure armoured with 16-tonne Tetrapods. The overland road behind the crest is located at D.L. (+) 4.10 m (D.L.: approximately lowest low water at Busan), and the nearest buildings are set back approximately 23 m from the crest [22]. The seaward face has a front slope of 1:1.5, reducing to 1:2 where a Tetrapod berm is present [12], and a crest width of approximately 5 m corresponding to two 2.5 m Tetrapods.

Following the severe overtopping and flooding during Chaba (2016), the Tetrapod armour was reinforced by stacking additional units along the seaward face, raising and strengthening the existing crest; because this reinforcement was applied unevenly along the structure, the reinforced Tetrapod crest lies locally below (Figure 6b) or above (Figure 6c) the seawall crest shown in the cross-section (Figure 6a). A representative crest elevation is therefore adopted for each event: the seawall crest of D.L. (+) 5.10 m for Typhoon Chaba (2016), and a section-averaged armoured-crest elevation of D.L. (+) 5.30 m for Typhoon Hinnamnor (2022). To represent the roughness of the Tetrapod armour, a nominal roughness reduction factor for Tetrapods (γ_f = 0.38 from Table 6.2 of EurOtop [17]) is adopted as a baseline value that is then adjusted to the local forcing and structure conditions (Section 2.2.3). The structural parameters are summarised in Table 1.

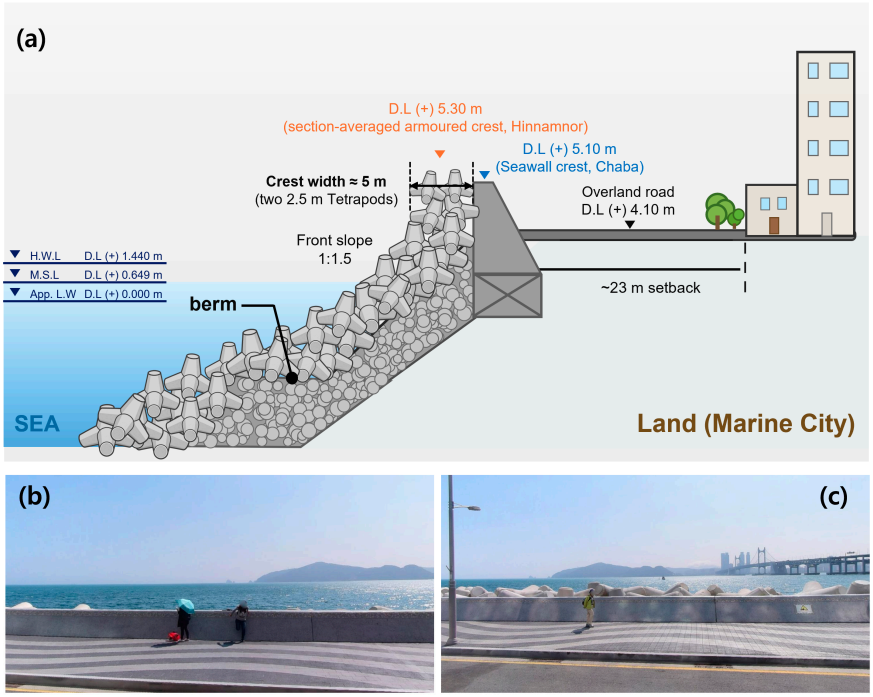


Figure 6. Cross-section of the coastal dike and the along-structure variation of Tetrapods in the study area: (**a**) representative cross-section of the coastal dike; (**b**) a section where the reinforced Tetrapod armour remains below the concrete crest; and (**c**) a section where the reinforced Tetrapod armour rises above the concrete crest.

Table 1. Structural specifications of the coastal structure fronting Marine City.

Parameter	Value
Armour units	16-tonne Tetrapods
Front slope	1:1.5 (Tetrapod); 1:2 (Tetrapod with berm)
Crest elevation—Chaba (2016)	D.L (+) 5.10 m (seawall)
Crest elevation—Hinnamnor (2022)	D.L (+) 5.30 m (section-averaged)
Crest width	5 m (two 2.5 m Tetrapods)

3.2. Typhoon Events: Chaba (2016) and Hinnamnor (2022)

Typhoon Chaba (2016) originated as a small tropical storm to the east of Guam on 28 September 2016, with a central pressure of 1000 hPa and a maximum wind speed of 18 m/s, and it intensified steadily as it tracked northward. By the morning of 5 October, it had developed into a strong, medium-sized typhoon with a central pressure of 955 hPa and a maximum wind speed of 40 m/s. Passing along the south-eastern coast of the Korean Peninsula, Chaba generated strong winds and storm surge along the southern coast. Representative observations in the nearby Busan coastal waters recorded significant wave heights of approximately 8 m and significant wave periods of approximately 10 s near the peak of the event [23]. In the study area, the superposition of strong winds and high waves caused severe damage, including the destruction of waterfront roads, wave overtopping of coastal structures, and flooding of low-lying areas (Figure 7a).

Typhoon Hinnamnor (2022) formed from a tropical depression over the western North Pacific to the south-east of Japan on 28 August 2022 and rapidly intensified to become the first super typhoon of the year. It reached its peak intensity on 30 August, with a minimum central pressure of 920 hPa and a maximum wind speed of approximately 54 m/s. At landfall, it had a central pressure of approximately 950 hPa and maximum winds near 45 m/s. As the storm passed Busan, it generated very high waves, elevated storm surge,

and torrential rainfall along the south-eastern coast. Representative observations in the nearby Busan coastal waters recorded significant wave heights of approximately 7 m and significant wave periods of approximately 10 s near the peak of the event [22]. At Marine City, the combination of high waves and elevated water levels again drove wave overtopping and inundation of the waterfront (Figure 7b).

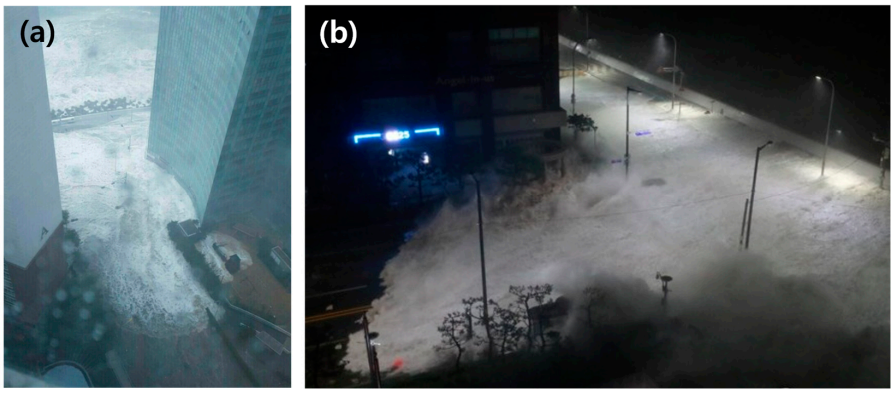


Figure 7. Wave overtopping and coastal flooding at Marine City during (**a**) Typhoon Chaba (2016) and (**b**) Typhoon Hinnamnor (2022).

4. Numerical Model Setup

In this study, the SCHISM-WWM model coupled with the EurOtop overtopping module was set up to evaluate the coastal flooding induced by wave overtopping. The coupled system computes the mean overtopping discharge at an interval of 120 s and transfers it to the inland domain, so that the wave overtopping-induced flooding processes are reproduced within a single computational mesh. In the present coupling, this mean discharge is re-evaluated at each coupling step as wave height, wave period, wave direction, and water level vary. The coupling interval therefore determines how frequently the mean discharge is updated, rather than the period over which it is averaged, and wave-by-wave variability and instantaneous peak discharges are not resolved. The unstructured triangular grid was designed with a spatially variable resolution ranging from approximately 45 km in the open ocean to approximately 5 m in the target area of Marine City, comprising 1,153,782 elements and 613,128 nodes. The model was configured in a two-dimensional, depth-averaged mode over a computational domain extending from 114° to 147° E and from 18° to 52° N (Figure 8).

Along the Marine City frontage, the coastal dike was discretised into a series of paired extraction and injection nodes (Section 2.1), each carrying the structure attributes required by the overtopping module: structure type, crest elevation, front slope, orientation, and armour roughness class (Table 1). Consistent with its classification as an armoured sloping structure, the coastal dike was assigned the rubble mound slope formulation, with the Tetrapod roughness factor evaluated dynamically from the local sea state (Section 2.2.3) and the crest-width attenuation applied across its width (Section 2.3.2), while the wave direction factor was computed at each node from the angle between the computed wave direction and the locally defined structure orientation (Section 2.2.2).

Atmospheric forcing was provided by the GDAS dataset (0.25° × 0.25° resolution, 3-hourly). The ocean boundary conditions were specified using the GLORYS12v1 reanalysis (0.08° × 0.08°) for water level and currents, together with the global WW3 hindcast (0.4° × 0.4°, CAWCR) for waves. Tidal forcing was imposed from the FES2014 dataset using eleven constituents (M2, S2, O1, K1, N2, K2, P1, Q1, M4, MS4, and MN4). Bottom friction was represented by the Manning coefficient, with values of 0.023 over the ocean and 0.016 over land. The model bathymetry was constructed from GEBCO data for the surrounding

seas, supplemented by the detailed nearshore bathymetry and coastline provided by the Korea Hydrographic and Oceanographic Agency (KHOA). The simulation conditions are summarised in Table 2.

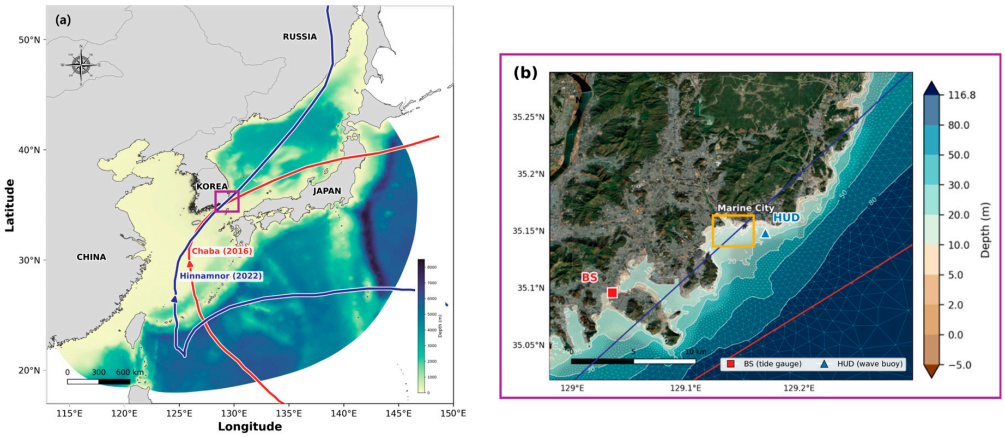


Figure 8. Computational domain of the SCHISM-WWM-EurOtop coupled model: (**a**) model bathymetry over the full domain with the tracks of Typhoon Chaba (2016) and Typhoon Hinnamnor (2022); (**b**) enlarged view of the Marine City area, Busan, showing the unstructured computational mesh, the water depth, the locations of the tide gauge (BS, red square) and the wave buoy (HUD, blue triangle), and the typhoon tracks near the study area (red line: Typhoon Chaba (2016); blue line: Typhoon Hinnamnor (2022)).

Table 2. SCHISM-WWM simulation conditions used in this study.

Model	SCHISM-WWM + developed EurOtop
Time step	120 s
Grid resolution	Max: 45 km, Min: 5 m (target area—Marine City); triangular unstructured grid
Grid	Elements: 1,153,782/Nodes: 613,128
Domain	114–147° E, 18–52° N
Vertical grid	2D (depth-averaged)
Atmospheric forcing	GDAS (0.25° × 0.25°), 3-hourly
Open boundary	GLORYS12v1 (0.08° × 0.08°); global WW3 hindcast (0.4° × 0.4°, CAWCR)
Tidal forcing	FES2014 (M2, S2, O1, K1, N2, K2, P1, Q1, M4, MS4, MN4)
Bed friction	Manning coefficient (ocean: 0.023, land: 0.016)
Simulation period	Chaba (2016): 24 September 2016 00:00–6 October 2016 00:00 UTC (including 10-day spin-up) Hinnamnor (2022): 26 August 2022 00:00–7 September 2022 00:00 UTC (including 10-day spin-up)

5. Results

5.1. Validation of External Forcing

To validate the external forcing during the passage of Typhoon Chaba (2016), the sea surface elevation and significant wave height computed by the SCHISM-WWM model were compared with observations from the Busan tide gauge (BS) and the Haeundae wave buoy (HUD) as shown in Figure 8b. The validation period was set from 01:00 UTC on 4 October to 13:00 UTC on 5 October 2016. Sea surface elevations and other model outputs reported in this section are referenced to mean sea level (MSL). The observed peak sea surface elevation (based on 1 h mean) was 125.1 cm (01:00 UTC, 5 October 2016), whereas

the modelled value was 110.1 cm (01:00 UTC, 5 October 2016), a difference of 15.0 cm (Figure 9a). The observed peak significant wave height at the Haeundae buoy (1 h mean) was 5.64 m (01:55 UTC, 5 October 2016), while the modelled value was 5.29 m (03:00 UTC, 5 October 2016), a difference of 0.35 m (Figure 9b). The observed spectral wave period at the Haeundae buoy (1 h mean) was 13.96 s (01:45 UTC, 5 October 2016), while the modelled value was 11.35 s (02:00 UTC, 5 October 2016), a difference of 2.61 s (Figure 9c). Because the observations were missing immediately after the typhoon passage, the observed maxima were determined from the interval preceding the data gap.

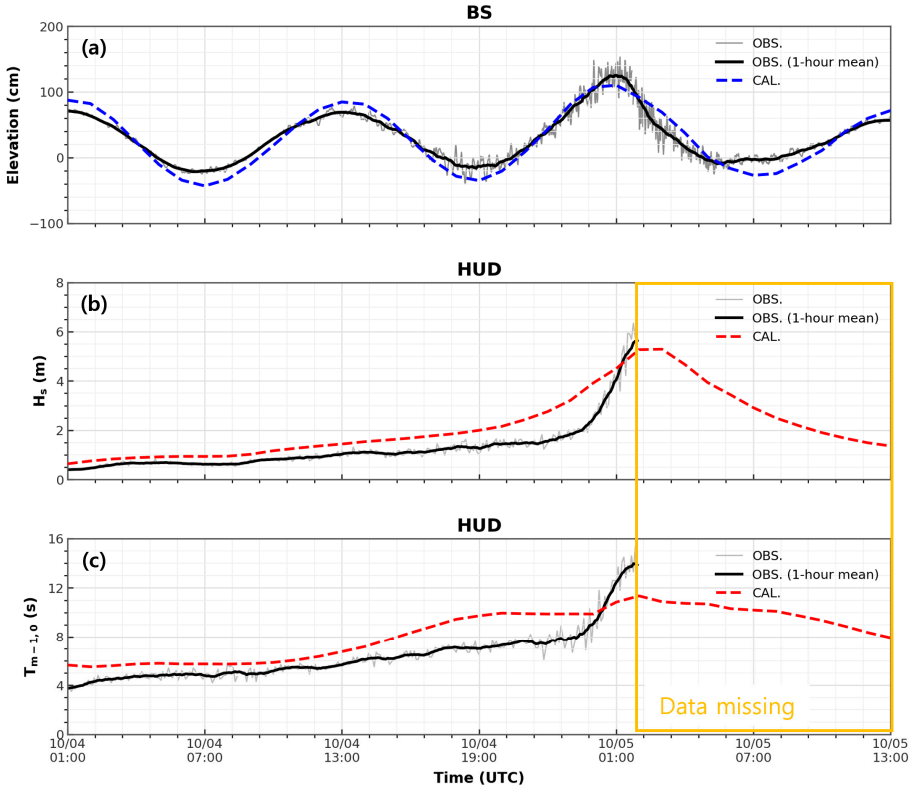


Figure 9. Comparison of observed and modelled time series during Typhoon Chaba (2016): (**a**) sea surface elevation; (**b**) significant wave height; (**c**) spectral wave period. Grey lines denote the raw observations, black lines the 1 h mean observations, and dashed lines the model results.

Typhoon Hinnamnor (2022) passed Busan on 5–6 September 2022, and the validation period was set from 20:00 UTC on 4 September to 08:00 UTC on 6 September 2022. The observed peak sea surface elevation (based on 1 h mean) was 118.0 cm (20:20 UTC, 5 September 2022), whereas the modelled value was 80.9 cm (20:00 UTC, 5 September 2022), a difference of 37.1 cm (Figure 10a). The observed peak significant wave height at the Haeundae buoy (1 h mean) was 6.07 m (19:00 UTC, 5 September 2022), while the modelled value was 6.33 m (20:00 UTC, 5 September 2022), an overestimation of 0.26 m (Figure 10b). The observed spectral wave period at the Haeundae buoy (1 h mean) was 12.41 s (18:09 UTC, 5 September 2022), while the modelled value was 12.09 s (21:00 UTC, 5 September 2022), a difference of 0.32 s (Figure 10c). As in the case of Typhoon Chaba (2016), the observations were missing immediately after the typhoon passage. Overall, the coupled model captured the temporal evolution and the timing of the storm-driven maxima in sea surface elevation, significant wave height, and spectral wave period under both events. It is therefore considered adequate as the external forcing for the subsequent overtopping-induced coastal flooding analysis.

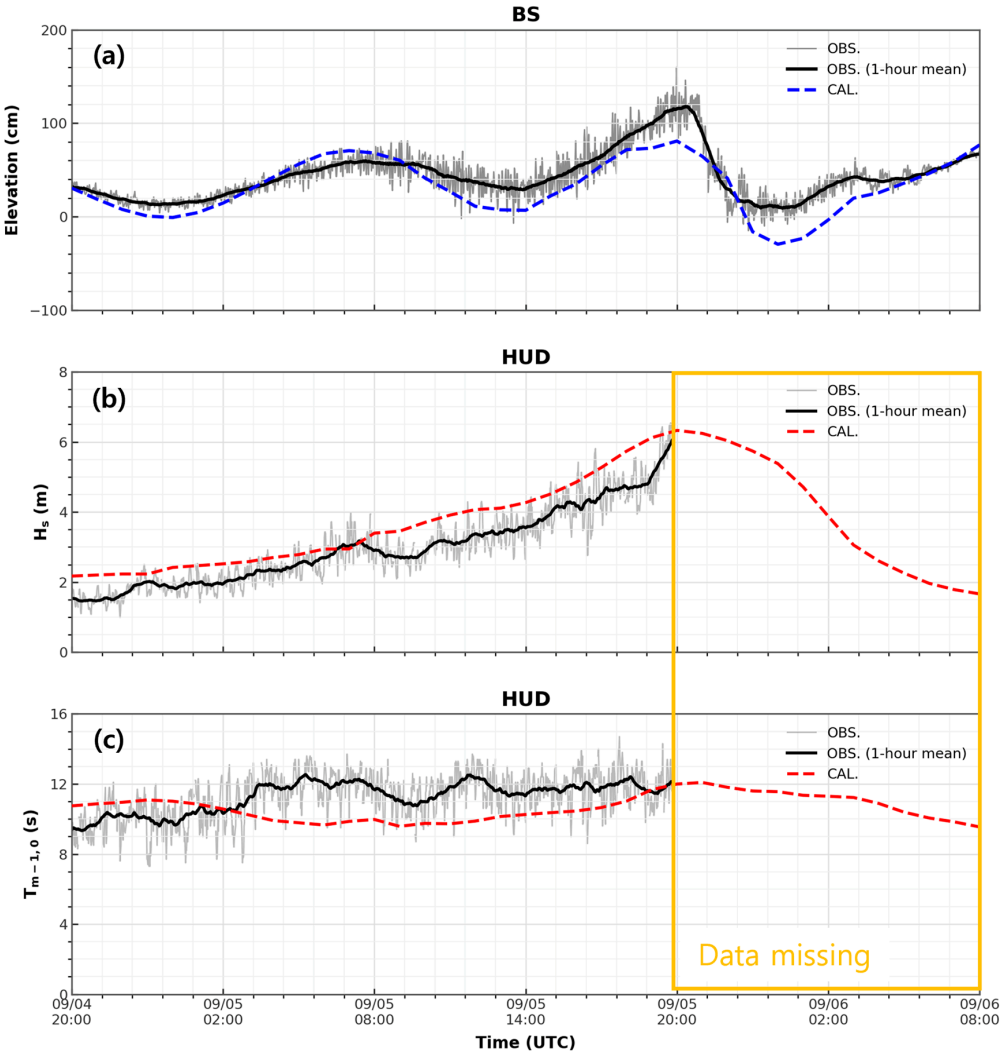


Figure 10. Comparison of observed and modelled time series during Typhoon Hinnamnor (2022): (**a**) sea surface elevation; (**b**) significant wave height; (**c**) spectral wave period. Grey lines denote the raw observations, black lines the 1 h mean observations, and dashed lines the model results.

5.2. Qualitative Evaluation of Overtopping Characteristics During Typhoon Hinnamnor (2022)

Since no quantitative inundation survey is available for Typhoon Hinnamnor (2022), the overtopping behaviour of the coupled model is evaluated qualitatively against the CCTV-based overtopping record reported by Jang and Yoon [22] for the Marine City seawall. Although the CCTV record cannot quantify the overtopping discharge, it provides a visual record of overtopping occurrence, allowing the modelled overtopping discharge to be compared with the observations in terms of the timing of occurrence and overtopping intensity.

Jang and Yoon [22] compiled the overtopping record from the CCTV footage of two shore-based broadcast cameras, the KBS camera [24] and the MBC camera [25], during the passage of the typhoon. As shown in Figure 11, the KBS camera covers the south-eastern segment (Area I), which extends from the eastern end of Area II to where the seawall begins to curve toward the south-east corner, and provides 12 h of footage from 09:00 to 21:00 UTC on 5 September. The MBC camera covers the southern segment (Area II), a short, straight stretch of seawall near the triangular road intersection, and provides 12 h of footage from 13:00 UTC on 5 September to 01:00 UTC on 6 September. In the model, these segments are identified by their structure node numbers and correspond to pair-nodes. From this footage, the number of overtopping events was counted at 30 min intervals, and each event was graded into High, Medium, and Low classes according to the overtopping height

(ζ) relative to the crest light-pole height (H_{lp} ≈ D.L. (+) 6.0 m—High ($\zeta > H_{lp}$), Medium ($0.5H_{lp} < \zeta < H_{lp}$), and Low ($\zeta < 0.5H_{lp}$)).

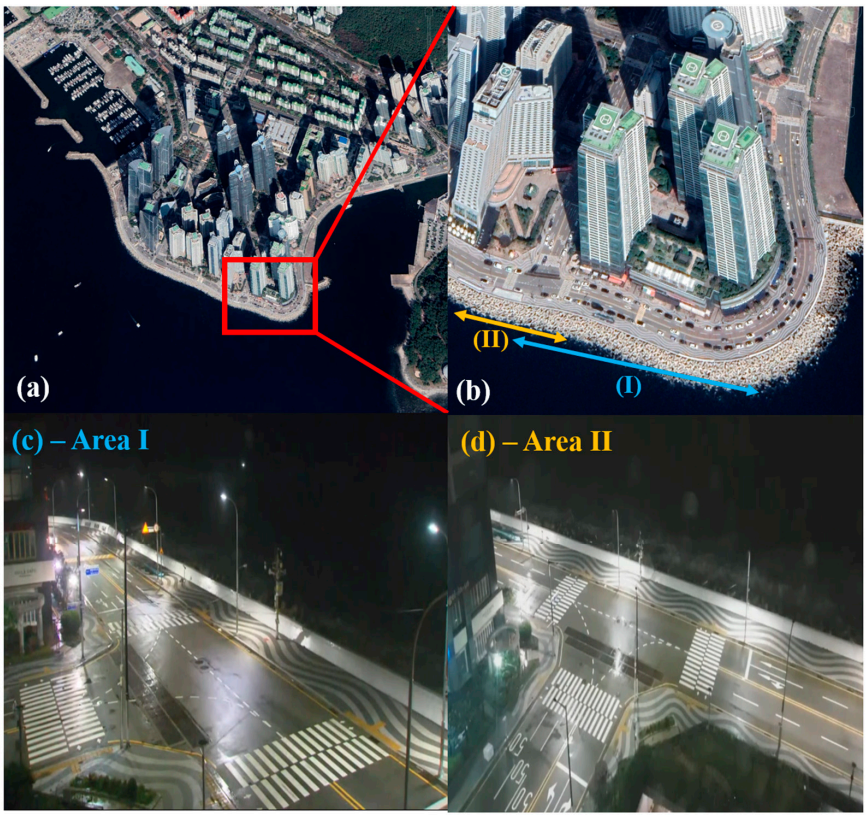


Figure 11. CCTV observation of wave overtopping at Marine City during Typhoon Hinnamnor (2022): (**a**) location of Marine City, Busan; (**b**) the monitored seawall showing the two camera-covered segments: Area I (KBS camera [24]) and Area II (MBC camera [25]); (**c**,**d**) CCTV views of Area I and II, respectively.

The temporal evolution of the modelled discharge and the observed occurrence counts is compared in Figure 12 for the two segments. In both areas the overtopping builds up from approximately 18:00 UTC on 5 September, reaches its maximum near 21:00 UTC, and then decays to near zero by about 23:00 UTC. The modelled discharge (solid line) closely follows the rise, peak, and decay of the CCTV occurrence counts (bars) in both Area I and Area II, so the model reproduces the timing of the observed overtopping maximum during the storm passage. The modelled discharge peak coincides with the tallest observed bin near 21:00 UTC in both areas, with the Area II peak occurring only slightly later than the Area I peak; in each segment the modelled and observed maxima fall within the same 30 min observation bin, so the peak timing is reproduced to within the temporal resolution of the record.

The intensity composition of the observed record is likewise consistent with the modelled discharge. In both Area I and Area II, low-intensity events occur almost continuously throughout the overtopping period, medium-intensity events make up the largest share of the counts, and high-intensity events appear only intermittently. The high-intensity events are not spread evenly through the event but concentrate in the bins around the 21:00 UTC peak—the same time at which the modelled discharge reaches its maximum—so the strongest overtopping in the model coincides with the most severe overtopping in the observations. The modelled discharge also follows the observed intensity reasonably well. In Area II, during the decay phase around 21:30 UTC, the occurrence count falls but the high-intensity share rises slightly, and the modelled discharge shows a correspondingly

small renewed rise rather than a steady decline, consistent with the model responding to the severity of the events and not only to their number.

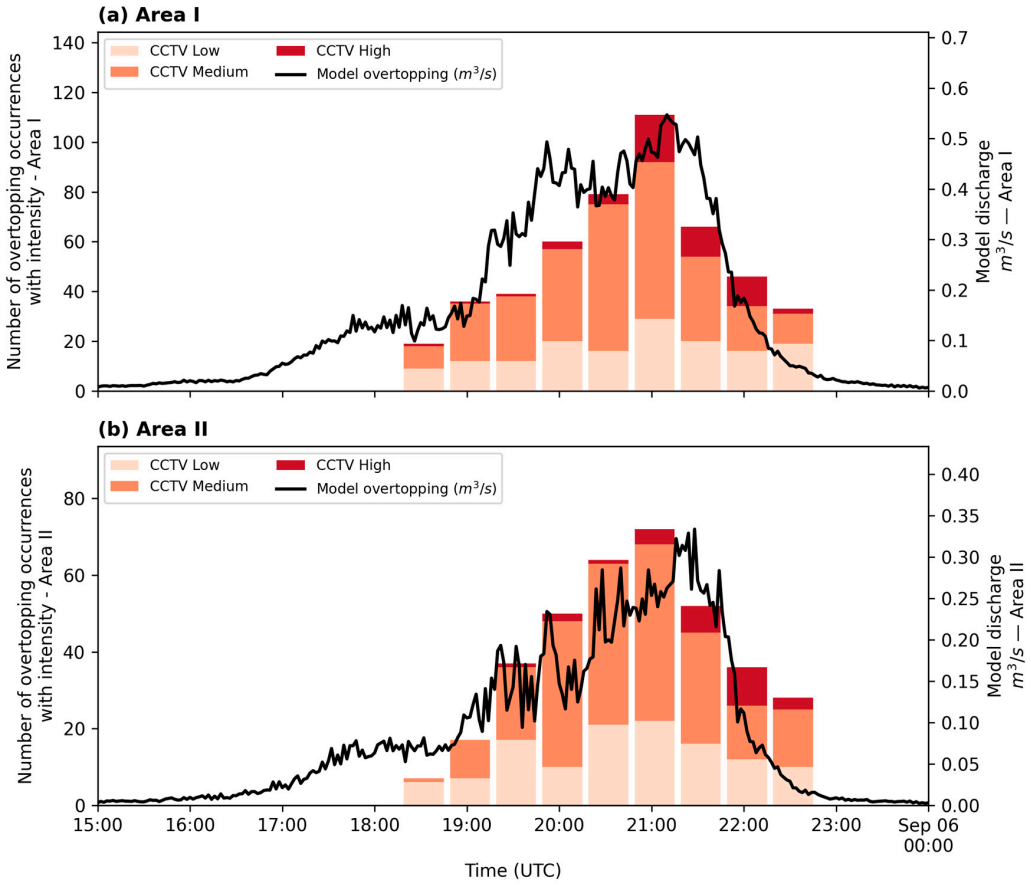


Figure 12. Temporal comparison of the modelled wave-overtopping discharge (solid line, right axis) and the CCTV-observed overtopping occurrence counts graded by intensity (stacked bars—Low, Medium, High; left axis) at the Marine City seawall during Typhoon Hinnamnor (5–6 September 2022, UTC): (**a**) Area I (south-eastern segment); (**b**) Area II (south segment).

Because the CCTV data are qualitative occurrence counts without absolute discharge or measured inundation depth, this evaluation is necessarily a pattern-based validation. It establishes the applicability of the module under a typhoon whose track and wave direction differ from those of Chaba (2016), and complements the quantitative inundation benchmark presented for Typhoon Chaba (2016) in Section 5.3.

5.3. Quantitative Validation of Overtopping-Induced Flooding During Typhoon Chaba (2016)

Inundation during an extreme event develops within a short time, and its depth and propagation are difficult to measure directly, so post-event water marks, drone footage, and CCTV records are commonly used for verification. For Typhoon Chaba (2016), the spatial distribution of the overtopping-induced flooding is validated against the field-based inundation traces reported by two studies (Lee et al. [5]; Suh and Kim [12]) for Marine City, which provide observed inundation depths at three and five survey points, respectively. Therefore, the surveyed data allows a quantitative point-by-point comparison with the modelled maximum inundation depth.

Figure 13a shows the observed inundation traces for the Chaba event. The field survey indicates inundation depths of approximately 70~80 cm along the front road ((1) and (2) points in Figure 13a) and relatively deeper inundation in the western part of Marine City,

where the lower ground elevation relative to the surroundings allowed the overtopped seawater to converge and accumulate.

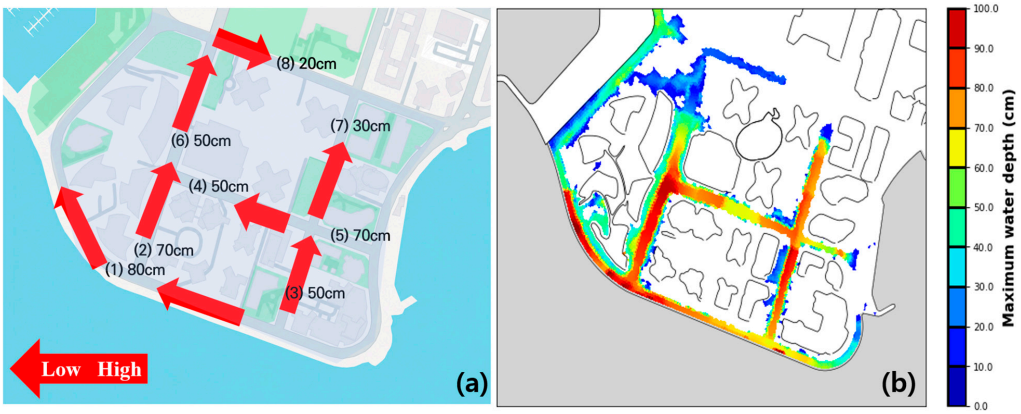


Figure 13. Comparison of the maximum inundation depth and extent at Marine City during Typhoon Chaba (2016): (**a**) field-based observed inundation traces with survey points, (**b**) modelled maximum inundation depth in this study.

The modelled maximum inundation depth and extent obtained in this study are shown in Figure 13b, and the quantitative comparison was carried out at the eight representative survey points (1)–(8) of Figure 13a (Table 3). Points (1), (3), and (4) are taken from Lee et al. [5], while points (2), (5), (6), (7), and (8) are taken from Suh and Kim [12]. The observed depths are 80, 70, 50, 50, 70, 50, 30, and 20 cm, while the model gives approximately 91, 73, 74, 67, 64, 63, 46, and 14 cm at each location. Averaged over the eight survey points, the mean absolute difference between the modelled and observed depths is approximately 12 cm, indicating reasonable overall agreement, while the model shows a tendency to overestimate the inundation depth. It should be noted that the observed depths were not measured directly during the flood. Instead, they were estimated afterwards from the water marks left on walls and structures, so some difference from the true peak water level is unavoidable in this comparison.

Table 3. Observed and modelled maximum inundation depths at the survey points of Figure 13a.

Survey Point	Source	Observed (cm)	Model (cm)	Difference (cm)
(1)	Lee et al. [5]	80	91	+11
(2)	Suh and Kim [12]	70	73	+3
(3)	Lee et al. [5]	50	74	+24
(4)	Lee et al. [5]	50	67	+17
(5)	Suh and Kim [12]	70	64	−6
(6)	Suh and Kim [12]	50	63	+13
(7)	Suh and Kim [12]	30	46	+16
(8)	Suh and Kim [12]	20	14	−6

The modelled spatial pattern of inundation is also consistent with the observations. The overtopped seawater converges in the lower-lying western district, where the deepest inundation forms, and decreases progressively toward the higher central and inland areas, producing a spatial contrast in inundation depth that follows the local ground elevation. This is reflected in the survey points, with the deeper inundation along the seaward front and in the hinterland immediately behind the structure (points (1) and (2)), and the shallower inundation toward the inner points (points (6), (7), and (8)). Although the validation relies on only eight survey points and the observations themselves are post-event estimates inferred from residual water marks, which inevitably carry some error, the

point-by-point comparison and the overall spatial pattern of inundation together indicate that the developed coupled model reproduces overtopping-induced flooding well.

The tendency of the model to overestimate the inundation depth may be partly attributable to the absence of an urban drainage network in the present coupling. The hinterland of Marine City is served by storm-sewer networks that discharge directly to the sea through several outfalls [5]. During Typhoon Chaba (2016), the accompanying rainfall was small [5], so the rainfall-runoff inflow into the storm sewers would have been limited and the flow within the conduits would have been largely contributed to by the wave overtopping. In that case, part of the overtopped water on the roads would have been conveyed back to the sea through these storm sewers, so that, before the sewer conduits became saturated, the resulting inundation would be smaller than that obtained from the present model. Because the present coupled system does not yet represent this drainage and discharge network, the overtopped water is retained on land instead of being partly evacuated, and the modelled inundation therefore tends to be overestimated relative to the observations.

6. Conclusions

This study developed EurOtop-based wave-overtopping modules within the cross-scale SCHISM-WWM modelling framework and applied it to Marine City, Busan, South Korea, a densely urbanised coast repeatedly damaged by overtopping-induced flooding. At every model time step, the module extracts the local water level and wave conditions at the seaward side of each coastal-structure pair-node, computes the mean overtopping or overflow discharge from the EurOtop formulae, and injects the resulting discharge at the landward side as a source term for inland flood propagation. The formulation additionally considers the wave-direction effect from the local structure orientation, applies a roughness reduction that depends on the armour type together with the structure slope and the wave steepness, and treats crest-width transfer losses, so that the overtopping responds to the spatially varying wave field and to the geometry of the structure rather than to a single representative condition.

The coupled model was evaluated against two past typhoons. For Typhoon Hinnamnor (2022), the modelled overtopping discharge was compared qualitatively with the CCTV-based overtopping record. The model reproduced both the observed temporal evolution and the intensity composition of the overtopping, indicating that the module responds to the severity of the overtopping events and not merely to their frequency.

For Typhoon Chaba (2016), the modelled maximum inundation depth was validated quantitatively against the field-based inundation traces at eight survey points. The modelled depths agreed reasonably with the observations, with a mean absolute difference of approximately 12 cm, and reproduced the observed spatial pattern, in which the overtopped seawater converges in the lower-lying western district where the deepest inundation forms, and decreases toward the higher central and inland areas. These validations show that the coupled model captures both the temporal evolution of overtopping and the spatial distribution of the resulting inundation.

Since the observed inundation depths used in the present study are post-event estimates available at only a few locations, a more rigorous quantitative assessment would be possible if the model were compared with more accurate and denser in situ measurements. In addition, the present coupling does not yet represent the urban drainage network, so that part of the overtopped water that would otherwise be conveyed back to the sea through the storm sewers is retained on land. Drainage effects may be approximated by prescribing infiltration-rate sinks within the inundation domain, with spatially varying infiltration rates used as proxies for drainage capacity when detailed drainage-network information is

unavailable [26]. However, such an approach requires an appropriate site-specific drainage rate and cannot explicitly represent storm-sewer conveyance or sewer backflow. Since reliable drainage-capacity data were unavailable for the present study, no uncalibrated sink was applied. Coupling the overtopping module with a rainfall–runoff and storm-sewer model is therefore identified as a priority for future work. Since the EurOtop formulations are implemented as a module fully coupled within the SCHISM-WWM framework, the system can be linked with other modules and models. With the incorporation of these additional capabilities, the coupled overtopping-flooding framework can become a more realistic tool for assessing compound flooding in urbanised coastal cities protected by artificial structures.

Author Contributions: Conceptualisation, H.J. and J.P.; methodology, H.J.; software, H.J.; validation, H.J. and S.J.; formal analysis, H.J.; investigation, H.J.; resources, J.P.; data curation, H.J. and S.J.; writing—original draft preparation, H.J.; writing—review and editing, H.J., J.P., S.J., and H.C.; visualisation, H.J. and S.J.; supervision, J.P. and H.C.; project administration, J.P.; funding acquisition, J.P. and H.C. All authors have read and agreed to the published version of the manuscript.

Funding: This research was supported by the Korea Institute of Marine Science & Technology Promotion (KIMST), funded by the Ministry of Oceans and Fisheries, Korea (RS-2025-02217872).

Data Availability Statement: The data presented in this study are available on request from the corresponding author.

Conflicts of Interest: All authors are employed by Geosystem Research Inc. The authors declare that the research was conducted in the absence of any commercial or financial relationships that could be construed as a potential conflict of interest.

References

1. Jo, J.; Kim, S.; Mori, N.; Mase, H. Combined storm surge and wave overtopping inundation based on fully coupled storm surge-wave-tide model. *Coast. Eng.* **2024**, *189*, 104448. [CrossRef]
2. Lee, H.Y.; Suh, S.W. Application of EurOtop to improve simulations of coastal inundations due to wave overtopping. *J. Coast. Res.* **2016**, *75*, 1377–1381. [CrossRef]
3. Higuera, P.; Lara, J.L.; Losada, I.J. Three-dimensional interaction of waves and porous coastal structures using OpenFOAM. Part I: Formulation and validation. *Coast. Eng.* **2014**, *83*, 243–258. [CrossRef]
4. Buccino, M.; Di Leo, A.; Tuozzo, S.; Còrdova Lopez, L.F.; Calabrese, M.; Dentale, F. Wave overtopping of a vertical seawall in a surf zone: A joint analysis of numerical and laboratory data. *Ocean Eng.* **2023**, *288*, 116144. [CrossRef]
5. Lee, S.; Kang, T.; Sun, D.; Park, J.-J. Enhancing an analysis method of compound flooding in coastal areas by linking flow simulation models of coasts and watershed. *Sustainability* **2020**, *12*, 6572. [CrossRef]
6. Lashley, C.H.; Zanuttigh, B.; Bricker, J.D.; van der Meer, J.; Altomare, C.; Suzuki, T.; Roeber, V.; Oosterlo, P. Benchmarking of numerical models for wave overtopping at dikes with shallow mildly sloping foreshores: Accuracy versus speed. *Environ. Model. Softw.* **2020**, *130*, 104740. [CrossRef]
7. Wang, Y.; Goodall, J.L.; Kumar, C.; McSpadden, D.; Barbosa, S.A.; Roy, B.; Shahabi, A.; Tahvildari, N. A hybrid CNN-LSTM surrogate model for hyper-resolution spatiotemporal flood forecasting in Norfolk, Virginia. *J. Hydrol. Reg. Stud.* **2026**, *64*, 103234. [CrossRef]
8. Anik, M.S.B.M.; An, C.; Li, S.S. Evolution from the physical process-based approaches to machine learning approaches to predicting urban floods: A literature review. *Environ. Syst. Res.* **2025**, *14*, 15. [CrossRef] [PubMed]
9. Jo, J.; Kim, S.; Kim, J.; Mori, N. Coastal and pluvial compound flooding of surge, wave, tide, rainfall-runoff, sewer flow, and seawall failure at coastal urban areas. *J. Hydrol.* **2025**, *661*, 133698. [CrossRef]
10. Dugor, J.; Rihouey, D.; Lang, P. Flood modelling on Île de Ré during Xynthia. In Proceedings of the 21st TELEMAC-MASCARET User Conference, Grenoble, France, 15–17 October 2014; pp. 27–34.
11. Saulnier, J.-B.; Paquereau-Gaboreau, T.; Delemasure, J.-V. Implementation of overtopping discharges in a 2D coastal flood model of the Mont Saint-Michel Bay. In Proceedings of the 2020 TELEMAC-MASCARET User Conference, Antwerp, Belgium, 14–15 October 2021; pp. 73–80.
12. Suh, S.W.; Kim, H.J. Simulation of wave overtopping and inundation over a dike caused by Typhoon Chaba at Marine City, Busan, Korea. *J. Coast. Res.* **2018**, *85*, 711–715. [CrossRef]

13. Ye, F.; Zhang, Y.J.; Yu, H.; Sun, W.; Moghimi, S.; Myers, E.; Nunez, K.; Zhang, R.; Wang, H.V.; Roland, A.; et al. Simulating storm surge and compound flooding events with a creek-to-ocean model: Importance of baroclinic effects. *Ocean Model.* **2020**, *145*, 101526. [CrossRef]
14. Park, K.; Di Lorenzo, E.; Zhang, Y.J.; Wang, H.; Ezer, T.; Ye, F. Delayed coastal inundations caused by ocean dynamics post-Hurricane Matthew. *npj Clim. Atmos. Sci.* **2024**, *7*, 5. [CrossRef]
15. Zhang, Y.J.; Ye, F.; Stanev, E.V.; Grashorn, S. Seamless cross-scale modeling with SCHISM. *Ocean Model.* **2016**, *102*, 64–81. [CrossRef]
16. Roland, A. Development of WWM II: Spectral Wave Modelling on Unstructured Meshes. Ph.D. Thesis, Technische Universität Darmstadt, Darmstadt, Germany, 2008.
17. Van der Meer, J.W.; Allsop, N.W.H.; Bruce, T.; De Rouck, J.; Kortenhaus, A.; Pullen, T.; Schüttrumpf, H.; Troch, P.; Zanuttigh, B. EurOtop: Manual on Wave Overtopping of Sea Defences and Related Structures. An Overtopping Manual Largely Based on European Research, but for Worldwide Application, 2nd ed. 2018. Available online: www.overtopping-manual.com (accessed on 26 June 2026).
18. Hughes, S.A.; Nadal, N.C. Laboratory study of combined wave overtopping and storm surge overflow of a levee. *Coast. Eng.* **2009**, *56*, 244–259. [CrossRef]
19. Christensen, N.F.; Røge, M.S.; Thomsen, J.B.; Lykke Andersen, T.; Burcharth, H.F.; Nørgaard, J.Q.H. Overtopping on rubble mound breakwaters for low steepness waves in deep and depth limited conditions. *Coast. Eng. Proc.* **2014**, *34*, 6. [CrossRef]
20. Eldrup, M.R.; Andersen, T.L.; Van Doorslaer, K.; Van der Meer, J. Improved guidance on roughness and crest width in overtopping of rubble mound structures along EurOtop. *Coast. Eng.* **2022**, *176*, 104152. [CrossRef]
21. Besley, P. *Wave Overtopping of Seawalls: Design and Assessment Manual*; R&D Technical Report W178; Environment Agency: Bristol, UK, 1999.
22. Jang, S.C.; Yoon, H.S. Characteristics of Wave Overtopping Generation over seawall at Busan Haeundae Marine City During Typhoon Hinnamnor. *J. Korean Soc. Mar. Environ. Energy* **2023**, *26*, 171–182. (In Korean) [CrossRef]
23. Yoon, H.S.; Park, J.H.; Jeon, Y.H. A study on wave overtopping of the seawall at Haeundae Marine City during the passing of Typhoon Chaba. *J. Korean Soc. Mar. Environ. Energy* **2017**, *20*, 152–159. (In Korean) [CrossRef]
24. KBS LIVE. Real-Time Situation at Haeundae Marine City, Busan, as Typhoon Hinnamnor Passes. *YouTube*. 6 September 2022. Available online: https://www.youtube.com/watch?v=DXnOwF7ROlM (accessed on 26 June 2026).
25. MBC LIVE. 'Typhoon Hinnamnor' Wave-Overtopping Damage at the Marine City Coastal Road, Busan—Live Footage. *YouTube*. 6 September 2022. Available online: https://www.youtube.com/watch?v=6FIQJ5QOmD8 (accessed on 26 June 2026).
26. Huang, W.; Zhang, Y.J.; Liu, Z.; Yu, H.-C.; Liu, Y.; Lamont, S.; Zhang, Y.; Hirpa, F.; Li, T.; Baker, B.; et al. Simulation of compound flooding in Japan using a nationwide model. *Nat. Hazards* **2023**, *117*, 2693–2713. [CrossRef]

Disclaimer/Publisher's Note: The statements, opinions and data contained in all publications are solely those of the individual author(s) and contributor(s) and not of MDPI and/or the editor(s). MDPI and/or the editor(s) disclaim responsibility for any injury to people or property resulting from any ideas, methods, instructions or products referred to in the content.